Breaking of internal Kelvin waves shoaling on a slope

Keisuke Nakayama[1]*, Takahiro Sato[2], Kojiro Tani[1], Leon Boegman[3], Ichiro Fujita[1] and Tetsuya Shintani[4]

[1] Graduate School of Engineering, Kobe University, Kobe, Japan.

[2] Energy System & Plant Engineering Company, Kawasaki Heavy Industries, Ltd., Kobe, Japan.

[3] Department of Civil Engineering, Queen's University, Kingston, Canada.

[4] Faculty of Urban Environmental Sciences, Tokyo Metropolitan University, Hachioji, Japan.

* *Corresponding author: K Nakayama*
Tel: +81788036056
E-mail: nakayama@phoenix.kobe-u.ac.jp
Address: Graduate School of Engineering, Kobe University, 1-1 Rokkodai-cho Nada-ku, Kobe city, 658-8501, Japan

Running title: Breaking of internal Kelvin waves shoaling on a slope

Key points:

- A coastal-jet was shown to occur at the lateral wall of a cyclonically-propagating internal Kelvin wave breaking over a uniform slope.
- The coastal-jet occurred under a geostrophic balance and generated an oblique downdraft running down the slope, due to Coriolis.
- An equation was formulated for estimating the residual current due to the coastal-jet.

Abstract

In stratified flow, breaking of internal waves over slopes induces resuspension of bottom sediments and transport of mass. When internal waves shoal and break, flow dynamics and mass transport differ greatly according to whether the Coriolis force is included or neglected. Despite its importance, the currents generated by breaking internal Kelvin waves remain uninvestigated. Therefore, this study considers breaking of internal waves over a uniform slope under Coriolis with equivalent upper- and lower-layer depths. Laboratory experiments, using a 6.0 m rotating tank, were undertaken to visualize currents using Particle Image Velocimetry. Experimental data validated a three-dimensional fluid dynamics model, in-which a coastal-jet was simulated to occur at the lateral wall (to the right) of the progressive internal Kelvin waves in the breaking zone; with generation of an oblique downslope return flow (downdraft) under Coriolis. The coastal-jet was driven by the geostrophic balance, and the equation for estimating the residual current, due to the jet, was formulated. The results provide insight on mass transport in lakeshore and coastal zones.

Keywords: Coriolis; geostrophic balance; coastal-jet; laboratory experiment; oblique downdraft; residual current

Introduction

In lakes and the ocean, breaking of internal waves over slopes plays an important role in resuspension and transport of mass (e.g., Wuest and Lorke, 2003; Lamb, 2014; Boegman and Stastna, 2019). When internal waves shoal and break, the breaking induces resuspension of bottom sediments (Gloor et al., 1994; Pierson and Weyhenmeyer, 1994; Steinman et al., 1997; Moum et al. 2003). Residual currents, from internal wave shoaling, cause long-term sediment transport, which affects biogeochemistry in coastal areas (Hosegood et al. 2004; Boegman and Ivey 2009; Aghsaee et al. 2015; Klymak and Moum, 2003; Scotti and Pineda, 2004; Davis and Monismith, 2011; Walter et al., 2012).

For example, Pineda (1994) found that internal bores, from breaking of internal waves, periodically influenced onshore transport of neustonic larvae in Southern California, Sandstrom & Elliott (1984) suggested the occurrence of several large wave-shoaling events per tidal cycle was sufficient to supply the required nutrients to the euphotic zone on the Scotian Shelf (Helfrich 1992), and Reeder et al. (2011) observed sand waves (amplitudes ≤16 m and wavelengths ≤350 m) on the continental formed by episodic shoaling of extreme internal solitary waves (ISWs) (>100-m amplitudes) during each lunar cycle. ISW breaking dynamics, including the formation of vortex cores during breaking, Derzo & Grimshaw (1997) is important for long-term mass transport (Lamb, 2002). The flow dynamics and mass transport will differ greatly according to whether the Coriolis force is included or neglected (Mortimer, 1952; Csanady, 1967; Hamblin, 1978; Maxworthy 1983; Melville et al. 1990; Asplin et al., 1999; Ingvaldsen et al. 1999; Helfrich, 2007; de la Fuente et al. 2008; Grimshaw and Helfrich, 2012).

Prior research that considers breaking of internal waves over a slope without Coriolis has demonstrated that the generation of high frequency internal waves, accompanying the change in water depth over the slope, plays an important role in the type of internal wave breaking (Helfrich, Melville & Miles, 1984; Helfrich and Melville, 2006; Nakayama et al., 2012). Boegman et al. (2005a) also showed that degeneration, from a low-frequency internal seiche to high-frequency ISWs is a significant factor, generating dynamic breaking in laboratory experiments using a tilting tank. Similarly, the laboratory experiments and analysis using the mKdV model by Horn et al. (2000;

2001; 2002) and the analysis using the fully-nonlinear and strongly-dispersive internal wave equations by Nakayama et al. (2019a) showed that degeneration from low to high frequency internal waves, through fission, will occur readily over a mild slope of < ~0.05 (Nakayama et al., 2019b).

Bourgault et al. (2014) found that mass transport from the breaking of ISWs over a slope differs according to the type of breaking. Boegman et al. (2005a) proposed an internal form of the Iribarren number, modified after Galvin (1968), and three types of breaking for ISWs in a two-layer laboratory system: spilling, plunging and collapsing breakers. Aghsaee et al. (2010) extended this work to include fission and demonstrated that computational results can be classified using bottom slope and wave slope. Sutherland et al. (2013), performed additional experiments and reconciled differences between the prior laboratory and numerical work, classifying both in terms of the internal Iribarren number. Nakayama et al. (2019b) proposed a new wave Reynolds number which can delineate plunging and collapsing breakers based on bottom slope and wave slope.

There are many studies related to breaking of internal waves in a two-layer system when the depths of the upper and lower layers are equivalent (e.g., Nakayama and Imberger, 2010). Nakayama and Imberger (2010) showed, in laboratory experiments, that collapsing breakers predominate regardless of layer depth, specific density ratios and wave slope. In general, collapsing breakers occur when the depths of the upper and lower layers are the same (over the flat bottom) using the critical depth, which is obtained from the nonlinear term of the KdV equation (Nakayama et al. 2019b).

It has long been known that internal wave dynamics vary greatly, when Coriolis effects are included. Helfrich (2007) successfully evaluated the decay of internal Kelvin waves (IKWs), by assuming that there is no change in the transverse direction in order to investigate ISWs with rotation in the ocean (Grimshaw et al., 2014). As the other example of ISWs with rotation, Shimizu and Nakayama (2017) also showed that bow-shaped ISWs propagate under the influence of the Earth’s rotation (Grimshaw et al., 2013), and soliton resonance for ISWs was found to occur with rotation. Maxworthy (1983) demonstrated that the transverse scales of the topography are not negligible for internal waves with rotation, in the oceanographic applications to sea straits and the continental shelves. Similarly, Melville et al. (1989 & 1990) investigated the amplitude decay of IKWs, propagating along the lateral wall of a channel.

The investigation of IKWs, with the presence of a lateral wall boundary, is of interest when determining long-term mass transport in the coastal boundary layer. For example, Antenucci & Imberger (2001) showed the importance of IKWs within the littoral zone of Lake Kinneret. Csanady (1975) found, through observation and theory, that IKW motion is one of the key factors controlling the coastal-jet in Lake Ontario (Csanady, 1972a and 1972b). Valipour et al. (2019) investigated nearshore/offshore connectivity resulting from IKWs in Lake Erie. For IKWs, in the presence of a lateral wall boundary, steepening occurs (Boegman et al., 2003), but production mechanisms of ISWs remains unclear with energy being lost to internal Poincaré waves (de la Fuente et al., 2008; Mortimer 2004). Moreover, research on steady state ISWs under Coriolis is lacking (Maxworthy 1983; Renouard et al., 1987; Melville et al. 1989; Melville et al. 1990); however, IKWs will be preferentially generated over ISWs, for small amplitude waves, when the depths of the upper and lower layers are equivalent and in the presence of a lateral wall boundary (Gill, 1982; Boegman et al., 2005b).

Therefore, as a first step to investigate breaking of internal waves over a slope considering Coriolis effects, it is necessary to study IKWs generated along the lateral wall when the depths of the upper and lower layers are equivalent. For the same case without Coriolis, a collapsing breaker will predominate over a uniform slope. A residual undertow, due to downdraft, will occur that drives an offshore bottom current from the littoral zone below the density interface and induces long-term mass transport (Nakayama and Imberger, 2010). However, an IKW progresses with a maximum amplitude at the lateral wall and the amplitude decreases greatly in the wall normal direction. Therefore, when Coriolis effects are considered, the mass transport mechanisms will likely differ from those revealed by Nakayama and Imberger (2010).

This study investigates how residual currents are generated when the water depths of the upper and lower layer are equivalent under Coriolis effects, using both laboratory experiments and numerical computations. In the laboratory experiments, a 6.0 m rotating tank was visualized using Particle Image Velocimetry (PIV). In the numerical computations, the Fantom model shown to have high reproducibility and accuracy in internal wave breaking by Nakayama et al. (2012) and Nakayama et al. (2019b), was applied to investigate the types of breaking of IKWs and residual currents under varying Coriolis conditions.

Method

Laboratory experiments

Laboratory experiments were carried out using a rotating tank with a length of 6.0 m, a width of 0.4 m, a water depth of 0.3 m. The tank was mounted on a rotating table with a width of 3.0 m and a length of 6.0 m at a height 1.0 m from the ground (Figure 1(b)). The bottom slope was 0.3 m / 2.0 m. By setting the length of the wave paddle to 0.7 m and the length of the nose-like airfoil to 0.5 m, the distance from the wave generation site to the end of the slope was 4.8 m. IKWs were generated by oscillating the wave paddle, which was first designed by Thorpe (1978) and used in the previous study by Nakayama and Imberger (2010). The nose-like airfoil was attached to prevent mixing adjacent to the area where the pycnocline intersects the airfoil. Density stratification was produced by slowly injecting salt water of ρ_2 = 1020 kg m^{-3} from two 0.03 m diameter holes in the bottom of the tank after filling with fresh water of ρ_1 = 1000 kg m^{-3} to the desired layer depth. Since IKWs have been shown to progress stably when the ratio of the upper- and lower-layer depths is 1, equivalent 0.15 m depths were specified for each layer. The thickness of the pycnocline was 0.02 m. In all experiments, the tank was spun-up for 30 minutes, so as to be in solid body rotation. From the layer thickness (= 0.15 m), viscosity (= 10^{-6} m^2 s^{-1}) and the Coriolis coefficient (= $4\pi/30$ s^{-1}), the timescale characterizing spin-down is estimated to be 756 s, showing that 30 minutes is sufficient. To make comparisons under the same conditions, the total cross-sectional flux, for producing IKWs, was made equivalent in all cases of the laboratory experiments and numerical computations.

For the laboratory experiments, case 'A' without Coriolis effects and case 'B2' with a Coriolis coefficient of $4\pi/30$ s^{-1} were carried out (Table 1). The period of IKWs, in both cases, was unified at 10.0 s, which corresponds to a wavelength of 1.2 m using a longwave celerity. The amplitude of internal waves in case A was set to 0.01 m, and the same total cross-sectional flux was given in case B2. To verify the computational results, the flow velocity was determined using PIV. The flow field was illuminated over horizontal length of 0.40 m and vertical height of 0.15 m on the right side of the IKW propagation direction using a Yag Laser (JAPAN LASER CORPOPATION, DPGL-2W) with a sheet thickness of 0.005 m (Figure 1(b)). The video camera (CASIO EX-100 Pro) resolution was 3840 x 2160 with a 30 s^{-1} frame rate (Fujita, 2002; Fujita and Maruyama, 2002). The flow was seeded with nylon crushed particles with a diameter of 80 μm and a specific gravity of 1.02. Since internal waves reach the slope 50 s after generation, PIV measurements were performed for 70 s (from 50 s to 120 s).

Numerical computations

A three-dimensional non-hydrostatic model, Fantom, was used to analyze the breaking of internal Kevin waves shoaling on the uniform slope. Fantom is an object-oriented parallel computing model that has been applied to analyze, not only real scale phenomena (Maruya et al., 2010; Nakamoto et al., 2013; Nakayama et al., 2014; Nakayama et al., 2016), but also laboratory scale phenomena (Nakayama et al, 2012; Nakayama et al., 2019b). Fantom is based on Direct Numerical Simulation (DNS) as well as a generic length-scale (GLS) equation model (Jones and Launder, 1972; Umlauf and Burchard, 2003), with a partial cell scheme used here to represent the uniform bottom slope in the z-coordinate bathymetry (Adcroft, 1997). Nakayama and Imberger (2010) computed a Kolmogorov scale of 0.56 mm, during collapsing breakers occurs over a uniform slope in a laboratory experiment, which is similar to case A. The vertical grid spacings, in this study, of 2.0 mm over the slope is 3.6 of the Kolmogorov scale and well within the grid limits for DNS (Moin and Mahesh, 1998). Arthur and Fringer (2014) further demonstrated that 9 times the Kolmogorov scale is sufficient of ISW breaking. Therefore, a sub-grid-scale closure scheme is not required in the present study.

The size of the computational domain was 4.5 m in length and 0.4 m in height, with a 0.3 m water depth and a slope of 0.3 m / 2.0 m (Figure 1(a)). To be consistent with laboratory experiments, we applied an initial hyperbolic tangent stratification:

$$\rho(z) = \rho_1 + \frac{\Delta\rho}{2}\left(1 + \tanh\frac{z - h_2}{0.5\alpha}\right) \tag{1}$$

where z is the upward-positive vertical coordinate with origin at equilibrium water surface, h_2 is the lower-layer thickness, ρ_1 is the density of the upper layer, $\Delta\rho$ is the density difference between the upper and lower layers, and α (= 0.02 m) is the thickness of the pycnocline.

We considered the case with a lower-layer density ρ_2 = 1020 kg m^{-3} and an upper-layer density ρ_1 = 1000 kg m^{-3}. IKWs were initialized with the theoretical solution of the flux with a phase of π in the upper and lower layer (left of Figure 1(a)). As in the laboratory experiments, the amplitude of IKWs in case A, without Coriolis, was set to 0.01 m and the other computations with Coriolis were performed by giving the same total cross-section flux in all cases:

$$U_{upper} = \frac{\varepsilon g a}{c_0} \exp\left(-\frac{f_C}{c_0} y\right) \sin\left(\frac{2\pi t}{t_i}\right) \tag{2}$$

$$U_{lower} = -U_{upper} \tag{3}$$

$$\varepsilon = \frac{\rho_2 - \rho_1}{\rho_2} \tag{4}$$

$$a_0 = a_m \frac{B}{\lambda_I} \frac{1}{1 - \exp(B/\lambda_I)} \tag{5}$$

where U_{upper} is the flux in the upper layer, a_0 is the amplitude of an IKW at the lateral wall, g is the gravitational acceleration, c_0 is the celerity of internal Kelvin wave, f_C is the Coriolis parameter, y is the width coordinate, t is the time, t_i is the period of the internal Kelvin wave, a_m is the amplitude without Coriolis (= 0.01 m), B is the width of the tank, U_{lower} is the flux in the lower layer, and λ_I is the inertial deformation radius (= c_0 / f_C).

The horizontal mesh size in the vicinity of the wave generator was 0.04 m, with a mesh of 0.005 m given on the bottom slope where breaking of IKWs occurs. The vertical mesh was 0.01 m at the upper and lower ends and 0.002 m over the bottom slope. The computational time step was 0.01 s, which corresponds to a CFL condition of 0.24 based on a longwave celerity and the smallest mesh size. A free surface was applied to the top boundary and no-slip conditions were given on the bottom and lateral boundaries. To investigate the effect of the Coriolis force, 5 different conditions were given, with Coriolis coefficient of 4π/20 s^{-1}, 4π/30 s^{-1}, 4π/40 s^{-1}, 4π/80 s^{-1} and 4π/160 s^{-1} (Table 1).

As the long wave celerity was estimated to be 0.121 m s^{-1}, the minimum and maximum inertial deformation radii were 0.19 m, 0.29 m, 0.39 m, 0.77 m and 1.54 m for cases B1 to B5, respectively. The total computational time was set to 100 s, which reproduced the IKW reflecting from the slope and reaching the wave generator.

Results

Laboratory experiments

To visualize the internal wave motion, a sequence of 5 images were superimposed (Figures 2a to 2c and Figures 3a to 3c). For example, Figure 2a was made by superimposing the five particle images from 54 s to 54 + 4/30 s with an interval of 1/30 s, which enables the particle trajectory streaks to be visualized (shown by orange arrow). The location of the visualization was at y = 0.005 m, due to the thickness of a laser sheet. In the absence of the Coriolis force, the particle motions revealed a downdraft (Figure 2c), with vertical circulation formed by the shoaling front of the internal wave (Figure 2a), which ran up the slope (Figure 2b). The breaking type was confirmed to be a collapsing breaker by comparing with the collapsing breaker shown in Nakayama and Imberger (2010; their Fig. 6). We confirmed that a collapsing breaker occurred in the different vertical cross section and there was no change in a breaking type in the spanwise direction. In contrast when Coriolis was included, no strong downdraft over the slope was evident at y = 0.005 m (Figure 3c). The vertical circulation at the front was also weak compared to the no Coriolis case (Figure 3a) because the front circulation was strengthened by the downdraft in the case of no Coriolis (Figure 2a). The type of breaking, within the y = 0.005 m plane, was similar to a collapsing-surging breaker, which has a weaker vertical circulation at the front.

PIV was performed using the particle images (Figures 2a to 2c and Figures 3a to 3c). Following the particle images, strong downdraft was found to occur without Coriolis (Figures 4c). As a result of the collision of the downdraft and the front, strong vertical circulation was generated (Figure 4a). The front then ran-up over the slope and separated as a part of the downdraft (Figure 4b). When Coriolis was included, the downdraft did not form (Figure 5c). Thus, the front was revealed to have less vertical circulation and the run-up distance was larger than the no Coriolis case, because baroclinic energy converged on the lateral wall in case with Coriolis (Figures 4a and 5a). Overall, at the lateral wall the velocity with Coriolis was shown to be larger than the no Coriolis case. In the laboratory experiments, accurate visualization was only carried out at y = 0.005 m. It was difficult to visualize inside the rotating tank due to the presence of large spanwise velocities perpendicular to the visualization plane, resulting in out-of-plane motion though the laser sheet. Therefore, we relied on the numerical computations to further investigate breaking of IKWs under different Coriolis conditions.

Numerical computations

Collapsing breakers occurred at y = 0.005 m without Coriolis (case A), as in the laboratory experiments (Figures 2d, 2e and 2f). During shoaling, the downdraft from the previous wave established a circulation at the internal wave front, which ran-up over the slope, establishing a downdraft. Again, in case B2 when the IKW ran-up over the slope the breaking type was found to be collapsing-surging at y = 0.005 m and the thickness of the front was smaller than the no Coriolis case because downdraft was not evident at y = 0.005 m (Figures 3d, 3e and 3f). Good agreement was found between the DNS and velocity vectors from the laboratory experiments, for cases both with and without Coriolis (Figures 4 and 5). The time series of the horizontal velocity, around the breaking zone at x = 3.45 m with z = 0.15 m, yielded a correlation coefficient, R^2 = 0.92 showing the quantitative performance of the model relative to the laboratory experiments (Figure 5). In case B2, with a Coriolis coefficient of $4\pi/30$ s^{-1}, there was no clear evidence of a downdraft at y = 0.005 m after the IKW ran-up over the slope, which suggests that the lower layer fluid transported up-slope moved in the spanwise direction, during wave breaking, due to Coriolis with a return flow at a different y position. Furthermore, since the inertial deformation radius was 0.29 m that, shorter than the wavelength of IKWs, it was expected that Coriolis enhanced mass transport in the spanwise direction.

In order to investigate how Coriolis affected breaking of IKWs, we compared the spanwise pycnocline displacement for case A (without Coriolis) and cases B1 to B3 (with Coriolis coefficients of $4\pi/20$ s^{-1}, $4\pi/30$ s^{-1} and $4\pi/40$ s^{-1}; Figure 6). In case B1, where the Coriolis coefficient was the maximum and the amplitude at the lateral wall was the largest, the run-up distance was at its maximum and the breaker type was collapsing-surging (Figure 6b). The definition of breaking point used in Nakayama et al. (2012) was applied (vertical pressure gradient is zero), to investigate the influence of Coriolis on breaking (Figure 6). When Coriolis was neglected, breaking occurred at the point where the downdraft collided with the front; as shown in Nakayama et al. (2012; their Figure 6a). For case B, where Coriolis was considered, the breaking point moved in the upslope direction as y increased. Since the inertial deformation radius was 0.19 m in case B1, the amplitude became too small to break over the slope at y = 0.2 m (Figure 6b). In contrast, for cases B2 and B3, because the internal deformation radii were 0.29 m and 0.39 m, the IKW was found to break over the slope at y = 0.2 m. The location of the breaking point in case B3 was similar to the no Coriolis case, which suggests that Coriolis changes the breaking type in the spanwise direction. Cases B4 and B5 were omitted in Figure 6, because when the Coriolis coefficient is smaller and the internal deformation radius is larger, these showed the same tendency as case B3. In particular, in case B5 with the smallest Coriolis coefficient, we could confirm the clear occurrence of vertical circulation at the front, which can be seen under the no Coriolis case.

Residual current analysis

To investigate long-term mass transport, phase-averaged density distributions and velocities were calculated adjacent to the lateral wall over three-wave periods, from the third to the fifth wave after the IKW reached the slope. The phase-averaged pycnocline became thicker in all Coriolis cases compared to the no Coriolis case (Figure 7). The maximum thickness of the phase-averaged pycnocline occurred in case B1, where the amplitude at the lateral wall, was the maximum among all cases (Table 1). The thickness of the phase-averaged pycnocline decreased with the amplitude at the lateral wall (Figure 7). Cases B2 and B4 were omitted in Figure 7 because they showed the same rate of decrease of the phase-averaged pycnocline thickness from case B1 to case B5. Since energy damping due to the breaking of the IKW at the lateral wall becomes larger as the amplitude increases, there is the possibility that the thickness of the phase-averaged pycnocline increases from case B5 to case B1 are due to the strength of turbulence causing mixing during breaking of IKWs.

In the absence of Coriolis (case A) an upslope residual current was generated above the phase-averaged pycnocline and a downslope return flow beneath the phase-averaged pycnocline (residual undertow) to satisfy conservation of mass; as shown in Nakayama and Imberger (2010) (Figure 8a). When Coriolis was included, the residual current reached 0.03 m s-1 in case B1, which was much larger than the no Coriolis case, because of energy concentration at the lateral wall. The residual current, around the phase-averaged pycnocline, due to breaking of the internal Kelvin waves was found to be unidirectional, upslope from the offshore breaking point. The phase-averaged pycnocline elevation increased in the breaking zone (from x = 3.4 m to x = 3.6 m) with an increase in the Coriolis coefficient. Csanady (1975) theoretically demonstrated that IKWs play a strong role in generating the observed coastal-jets in Lake Ontario (Csanady, 1972a; Csanady, 1972b). Valipour et al. (2019) also showed that coastal-jets are generated in Lake Erie due to IKWs using field observations and a three-dimensional numerical model. Although IKW breaking is a key factor driving the unidirectional residual current in this study, we may also refer to the residual current as a 'coastal-jet' because the residual current is found to have the same unidirectional characteristics.

To analyze the coastal-jet in more detail, residual currents at z = 0.15 m and 1 mm above the slope are shown in Figure 9. In case A (no Coriolis), there was no change in the residual current in the spanwise direction (Figure 9a). However, a large difference in the spatial distribution of the residual current existed among all Coriolis cases (Figure 9b). In case B3, the magnitude and direction of the residual current changed greatly in the spanwise direction, which resulted in the absence of a strong residual current at y = 0.2 m at z = 0.15 m. Furthermore, in the residual current just above the slope, a downdraft was uniformly generated in the offshore direction without Coriolis (Figure 9c), but 'oblique downdraft' occurred under Coriolis (Figure 9d). The existence of the oblique downdraft, due to Coriolis, is expected to drive the coastal-jet around the phase-averaged pycnocline (Figure 8).

Discussion and Conclusions

The numerical computations showed that the maximum velocity of the coastal-jet, u_B, that occurred in case B1 was three times larger than that in case B5 (Table 1). To understand this great effect of IKW breaking on the coastal-jet, we computed the phase-averaged velocity at the lateral wall by only considering wave motion (Equation (2)). It was found that the phase-averaged velocity without IKW breaking was much smaller than the coastal-jet, which suggests that the coastal-jet was induced by IKW breaking (Figure 10). In other words, there may be a possibility that IKW breaking enhances the speed of a coastal-jet adjacent to the lateral wall within the breaking zone. It is well-known that such a phase-averaged current is associated with a mean surface elevation in terms of the radiation stress, in the depth-integrated momentum-flux. Therefore, by decomposing the pycnocline elevation and the flow velocity into components greater-than-and-equal-to and less-than-and-equal-to the IKW period, the equilibrium momentum balance relation in the spanwise direction within the breaking zone in the lower layer over the wave period can be obtained:

$$\underbrace{\overline{\frac{\partial v_I}{\partial \mathrm{t}} + u_I \frac{\partial v_I}{\partial \mathrm{x}} + v_I \frac{\partial v_I}{\partial \mathrm{y}}}}_{\text{negligible}} + \overline{f_C u_I} = -\overline{\varepsilon g \frac{\partial \eta_I}{\partial y}} - \underbrace{\overline{\frac{\rho_1}{\rho_2} g \frac{\partial \eta_S}{\partial y}}}_{\text{negligible}} \tag{6}$$

$$f_C u_B = -\varepsilon g \left.\frac{\partial \eta}{\partial y}\right|_{lateral\ wall} \tag{7}$$

Here the upper horizontal bar indicates the phase average, v_I is the velocity in y direction in the lower layer, u_I is the velocity in x direction in the lower layer, η_I is the pycnocline elevation, η_S is the water surface elevation, u_B is the phase-averaged velocity within the breaking zone adjacent the lateral wall and η is the phase-averaged pycnocline elevation in the breaking zone. This approach is similar to the theoretical investigation of baroclinic currents by Csanady (1979), in which geostrophic balance was important for the generation of baroclinic currents. Charney (1955) also showed the occurrence of a coastal-jet under the geostrophic balance.

A clear breaking zone was found in the range of x = 3.4 m to 3.5 m (Figures 6 and 7), and we computed $\partial\eta / \partial y$ at the lateral wall from the numerical computations. As a result, the velocity of the coastal-jet from Equation (7) agrees with the numerical computations, which shows that the geostrophic balance assumed in Equation (7) was established (Figure 10). Since it has been shown that a phase-averaged surface elevation drives mean flow under an oscillatory external force, such as radiation stress, the coastal-jet we obtained in this study is expected to be caused by an analogous effect, which is distinct in that Coriolis controls mean flow. It should be noted that the phase-averaged advection term and the spanwise change in the phase-averaged surface elevation were confirmed to be negligible from the numerical computations.

From the numerical simulations it is possible to readily obtain the spatial distribution of a phase-averaged pycnocline, and so we applied Equation (7) to successfully estimate the velocity of the coastal-jet. However, it will be difficult from field observations to estimate $\partial\eta\,/\,\partial y$ at lakeshore or the lateral boundary of a sea strait. Therefore, we modify Equation (7) by introducing a new parameter, the effective pycnocline elevation at the lateral wall η_{B0}, and assuming that the gradient of η in the y direction is associated with η_{B0} and an inertial deformation radius, λ_I. The velocity of the coastal-jet, u_B, can be modelled as a function of η_{B0} when f_C and c_0 are constant (Equation (9)).

$$\left.\frac{\partial\eta}{\partial y}\right|_{lateral\,wall} = \frac{\partial}{\partial y}\left[\eta_{B0}\exp\left(-\frac{1}{\lambda_I}y\right)\right]_{lateral\,wall} = -\frac{\eta_{B0}}{\lambda_I} \tag{8}$$

$$u_B = \frac{\varepsilon g \eta_{B0}}{f_C\lambda_I} = \frac{\varepsilon g \eta_{B0}}{c_0} \tag{9}$$

where η_{B0} is the effective pycnocline elevation at the lateral wall.

The unknown parameter, η_{B0}, can be obtained by comparing Equations (7) and (9) as follows:

$$\eta_{B0} = -\frac{c_0}{f_C}\left.\frac{\partial\eta}{\partial y}\right|_{lateral\,wall} \tag{10}$$

Since the parameter, η_{B0}, is expected to be associated with turbulence, following Nakayama and Imberger (2010) we evaluated the critical amplitude, describing the strength of turbulence in internal wave breaking, to normalize the amplitude of the IKWs at the lateral wall and made comparisons with η_{B0} (Equation (11)) (Figure 11):

$$a_C = C_S h_2 = \sqrt{\frac{8}{\pi B_P^5}}\,h_2 \tag{11}$$

$$B_P = \frac{2\omega_0}{f_S} \tag{12}$$

$$t_0 = \frac{l_0}{t_B} \tag{13}$$

$$t_0 = \frac{l_0}{t_B} \tag{13}$$

$$\omega_0 = \frac{2\pi t_0}{\sqrt{\varepsilon g a_0}} \tag{14}$$

where, a_C is the critical amplitude of internal wave breaking over a uniform slope, f_S is the breaking parameter over a uniform slope (= 0.9), t_B is the wave period of internal waves, l_0 is the horizontal length of a slope in the lower layer, and h_2 is the lower layer depth.

We found a_C = 0.00126 m, which is much smaller than the amplitude at the lateral wall, showing that in the absence of Coriolis the normalized amplitude $a_0 / a_C = 8$, which means that reflection from the slope can be ignored (Nakayama and Imberger, 2010). In case B5, where Coriolis was the smallest, the velocity of the coastal-jet was found to be almost the same as the offshore current in case A (no Coriolis) (Figure 8). In other words, when turbulence due to IKW breaking occurs under conditions where λ_I is larger than the wavelength of the IKW (1.2 m), the geostrophic balance may be negligible in the phase-averaged field and consequently the coastal-jet becomes similar to the offshore current under the no Coriolis case. Melville et al. (1990) similarly demonstrated the importance of Coriolis when the Rossby radius was smaller than the wavelength of an IKW (Csanady, 1975). In addition, it appears that η_{B0} / a_C is a linear function of a_0 / a_C (Figure 11). Therefore, the velocity of coastal-jet may be estimated using the following equation when λ_I is equal to or smaller than the IKW wavelength.

$$u_B = \beta \frac{\varepsilon g a_0}{c_0} \tag{15}$$

where β ~ 0.75 from Figure 11.

The proposed equations presented in this paper may allow predictions to be made for a coastal-jet in lakes and sea straits. As an example, we refer the results from a field study in Lake Erie by Valipour et al. (2019). They investigated two coastal-jets generated by IKWs in Lake Erie by deploying acoustic doppler current profilers and thermistor chains. One was a westward coastal-jet with a phase speed of 0.37 m s^{-1} in the eastern basin, and the other is also a westward coastal-jet with a phase speed of 0.22 m s^{-1} in the central basin. The specific density deference was about 0.0029 between a 5 °C hypolimnion and 25 °C epilimnion. The Estuary and Lake Computer Model (ELCOM) was applied to estimate the velocity of the coastal-jets to be ~ 0.3 m s^{-1} in the eastern basin and ~ 0.2 m s^{-1} in the shallower central basin. Valipour et al. (2015) measured the displacement of pycnocline in the central basin of Lake Erie to be < ~ 5 m. We may thus use Equation (15) to estimate the velocity of a coastal-jet in the central basin to be u_B = 0.10 m s^{-1}, 0.20 m s^{-1} and 0.30 m s^{-1} when the amplitudes of IKWs are 1.0 m, 2.0 m and 3.0 m, respectively, which reasonably agree with the velocity of the coastal-jets from ELCOM, 0.2 m s^{-1}. But, the computed velocity of the coastal-jets by ELCOM was also similar to the linear baroclinic phase speed. Therefore, further research is needed to confirm the generation mechanisms energizing coastal-jets.

Experiments on breaking of IKWs over a slope using a rotating tank showed that the presence of the Coriolis force drives collapsing-surging breakers adjacent to the lateral wall. The type of breaking changed, in the spanwise direction, when the depths of the upper and lower layers were the same; although collapsing breakers dominated when Coriolis was neglected. Using a three-dimensional DNS model, a coastal-jet was shown to occur adjacent to the lateral wall on the right side of the progressive IKWs under Coriolis. The coastal-jet was found to be driven by an oblique downdraft running down the slope due to Coriolis. Therefore, in addition to the existing theory on known mechanisms, a new mechanism to generate coastal-jets was proposed in this study characterized by IKW breaking.

Furthermore, an equation for estimating the residual current, due to the jet, was formulated, it was demonstrated that the normalized amplitude (a_0 / a_C) has a value of about 0.5 to 20 at field-scale (Nakayama and Imberger, 2010). It is possible for the range of (a_0 / a_C) to be from 6 to 20, to predict the occurrence of the coastal-jet, which may control long-term mass transport, using

Equation (15). Therefore, even when the thicknesses of the upper and lower layers are the same, it is important to collect additional data, in future, with different Coriolis coefficients and normalized amplitudes in order to verify Equation (15) for predicting u_B using f_C, a_0 / a_C and η_{B0}; especially the case when a_0 / a_C is from 0.5 to 6.0. Additionally, in the future, it is necessary to investigate the long-term mass transport due to IKWs under different upper- and lower-layer thicknesses.

Acknowledgments:

This work was supported by the Japan Society for the Promotion of Science under grant 18H01545 and 18KK0119. We thank to Y. Watanabe and K. Shimizu for helpful comments. The executable binary (windows, mac, linux) of the three-dimensional hydrodynamic model, Fantom, used in this study, is available from http://www.comp.tmu.ac.jp/shintani/fantom.html. The model outputs are available from https://github.com/kuaqua/JGR2019, "The model outputs for Nakayama et al. (2019)".

References

A. J. Adcroft and C. N. Hill and J. Marshall, Representation of topography by shaved cells in a height coordinate ocean model, Mon. Wea. Rev. 125, 2293-2315 (1997).

P. Aghsaee, L. Boegman and K. G. Lamb, Breaking of shoaling internal solitary waves, J. Fluid Mech. 659, 289-317 (2010).

P. Aghsaee and L. Boegman, Experimental investigation of sediment resuspension beneath internal solitary waves of depression, J. Geophys. Res. 120, 3301-3314, doi:10.1002/ 2014JC010401 (2015).

J. P. Antenucci, and J. Imberger, Energetics of long internal gravity waves in large lakes, Limnol. Oceanogr., 46, 1760–1773 (2001).

J.P. Antenucci, Currents in stratified water bodies 3: effects of rotation. Hydrodyn. Mix. 559–567 (2009).

R.S. Arthur and O.B. Fringer, The dynamics of breaking internal solitary waves on slopes, J. Fluid. Mech. 761, 360-398 (2014).

L. Asplin, A. G. V. Salvanes and J. B. Kristoffersen, Nonlocal wind - driven fjord‐coast advection and its potential effect on plankton and fish recruitment, Fish. Oceanogr., 8, 255-263 (1999).

L. Boegman and G. N. Ivey, Flow separation and resuspension beneath shoaling nonlinear internal waves, J. Geophys. Res. 114, C02018 (2009).

L. Boegman, G. N. Ivey and J. Imberger, The degeneration of internal waves in lakes with sloping topography, Limnol. Oceanogr. 50, 1620-1637 (2005a).

L. Boegman, G. N. Ivey, and J. Imberger. The energetics of large-scale internal wave degeneration in lakes. Journal of Fluid Mechanics. 531: 159-180 (2005b).

L. Boegman, J. Imberger, G. N. Ivey and J. P. Antenucci, High-frequency internal waves in large stratified lakes. Linmol. Oceanogr. 48(2) 895-919 (2003).

D. Bourgault, M. Morsilli, C. Richards, U. Neumeier and D. E. Kelley, Sediment resuspension and nepheloid layers induced by long internal solitary waves shoaling orthogonally on uniform slopes, Cont. Shelf Res. 72, 21-33 (2014).

J. G. Charney, The generation of oceanic currents by the wind, J. Mar. Res. 14, 477-498 (1955).

G. T. Csanady, Large-scale motion in the great lakes, J. Geophys. Res. 72(16), 4151-4162 (1967).

G. T. Csanady, The coastal boundary layer in Lake Ontario: Part II. The summer-fall regime, J. Phys. Oceanogr. 2, 168–176 (1972a).

G. T. Csanady, The coastal boundary layer in Lake Ontario. Part I: The Spring Regime, J. Phys. Oceanogr. 2, 41–53 (1972b).

G. T. Csanady, Hydrodynamics of large lakes, Annu. Rev. Fluid Mech. 7, 357-386 (1975).

G. T. Csanady and J. T. Scott, Baroclinic coastal jets in Lake Ontario during IFYGL, J. Phys. Oceanogr. 4, 524–541 (1974).

K. A. Davis and S. G. Monismith, The modification of bottom boundary layer turbulence and mixing by internal waves shoaling on a barrier reef, J. Phys. Oceanogr. 41(11), 2223-2241 (2011).

A. de la Fuente, K. Shimizu, J. Imberger and Y. Niño, The evolution of internal waves in a rotating, stratified, circular basin and the influence of weakly nonlinear and nonhydrostatic accelerations, Limnol. Oceanogr., 53, 2738–2748 (2008).

O. G. Derzho and R. Grimshaw, Solitary waves with a vortex core in a shallow layer of stratified fluid, Phys. Fluids. 9, 3378-3385 (1997).

A. de la Fuente, K. Shimizu, Y. Niño and J. Imberger, Nonlinear and weakly nonhydrostatic inviscid evolution of internal gravitational basin - scale waves in a large, deep lake: Lake Constance, J. Geophys. Res. 115, C12045 (2010).

I. Fujita, Particle image analysis of open-channel flow at a backward facing step having a trench, J. Visual. 5(4), 335-342 (2002).

I. Fujita and T. Maruyama, Hydraulic characteristics of open-channel flow downstream of a drop structure having a trench, J. Hydroscience Hydraul. Eng., 20(1), 103-111 (2002).

C. J. Galvin, Breaker type classification on three laboratory beaches, J. Geophys. Res. 73, 3651-3659 (1968).

A. Gill, Atmosphere-Ocean Dynamics, Volume 30, Academic Press, 662 (1982).

M. Gloor, A. Wüest, and M. Münnich, Benthic boundary mixing and resuspension induced by internal seiches, Hydrobiologia 284, 59-68, doi:10.1007/BF00005731 (1994).

R. Grimshaw, C. Guo, K. Helfrich and E. R. Johnson, Experimental study of the effect of rotationon nonlinear internal waves, Phys Fluids. 25, 056602 (2013).

R. Grimshaw and K. R. Helfrich, The effect of rotation on internal solitary waves, IMA J. Appl. Math. 77(3), 326-339 (2012).

R. Grimshaw, C. Guo, K. Helfrich and V. Vlasenko, Combined effect of rotation and topography on shoaling oceanic internal solitary waves, J. Phys. Oceanogr. 44, 1116-1132 (2014).

P. F. Hamblin, Internal Kelvin waves in a Fjord lake, J. Geophys. Res. 83, 2409-2418 (1978).

K. R. Helfrich, Decay and return of internal solitary waves with rotation, Phys. Fluids. 19, 026601 (2007).

K. R. Helfrich, W. K. Melville and J. W. Miles, On interfacialsolitary waves over slowly varying topography, J. Fluid Mech. 149, 305-317 (1984).

K. R. Helfrich and W. K. Melville, Long nonlinear internal waves, Annu. Rev. Fluid Mech. 38, 395-425 (2006).

D. A. Horn, L. G. Redekopp, J. Imberger and G. N. Ivey, Internal wave evolution in a space–time varying field, J. Fluid Mech. 424, 279–301 (2000).

D. A. Horn, J. Imberger and G. N. Ivey, The degeneration of large-scale interfacial gravity waves in lakes, J. Fluid Mech. 434, 181-207 (2001).

D. A. Horn, J. Imberger, G. N. Ivey and L. G. Redekopp, A weakly nonlinear model of long internal waves in closed basins, J. Fluid Mech. 467, 269–287 (2002).

P. Hosegood, J. Bonnin and H. van Haren, Solibore-induced sediment resuspension in the Faeroe-Shetland Channel, Geophys. Res. Lett. 31, L09301, doi:10.1029/2004GL019544 (2004).

M. E. Inall, Internal wave induced dispersion and mixing on a sloping boundary, Geophys. Res. Lett. 36, L05604, doi:10.1029/2008GL036849 (2009).

R. Ingvaldsen, M. B. Reitan, H. Svendsen and L. Asplin, The upper layer circulation in Kongsfjorden and Krossfjorden-A complex fjord system on the west coast of Spitsbergen, Memoirs of NIPR, 54, 393-407 (1999).

W. P. Jones and B. E. Launder, The prediction of laminarization with a two-equation model of turbulence, Int. J. Heat Mass Transfer 15, 301-314 (1972).

J. M. Klymak and J. N. Moum, Internal solitary waves of elevation advancing on a shoaling shelf, Geophys. Res. Lett. 30(20), 2045, doi:10.1029/2003GL017706 (2003).

K. G. Lamb, A numerical investigation of solitary internal waves with trapped cores formed via shoaling, J. Fluid Mech. 451, 109-144 (2002).

K. G. Lamb, Internal Wave Breaking and Dissipation Mechanisms on the Continental Slope/Shelf, Annu. Rev. Fluid Mech. 46, 231-254 (2014).

Y. Maruya, K. Nakayama, T. Shintani and M. Yonemoto, Evaluation of entrainment velocity induced by wind stress in a two-layer system, Hydrological Research Letters 4, 70-74 (2010).

T. Maxworthy, Experiments on solitary internal Kelvin waves, J. Fluid Mech. 129, 365-383 (1983).

W. K. Melville, G. G. Tomasson and D. P. Renouard, On the stability of Kelvin waves, J. Fluid Mech. 206, 1-23 (1989).

C. H. Mortimer, Water movements in lakes during summer stratification: Evidence from the distribution of temperature in Windemere, Phil. Trans. R. Soc. Lond. A Math. Phys. Sci. 236, 355–404 (1952).

C. H. Mortimer, Lake Michigan in Motion: Responses of an Inland Sea to Weather, Earth-spin, and Human Activities, University of Wisconsin Press (2004).

P. Moin and K. Mahesh, Direct numerical simulation: a tool in turbulence research, Annu. Rev. Fluid. Mech. 30, 539-578 (1998).

J. N. Moum, D. M. Farmer, W. D. Smyth, L. Armi and S. Vagle, Structure and generation of turbulence at interfaces strained by internal solitary waves propagating shoreward over the continental shelf, J. Phys. Oceanogr. 33, 2093-2112 (2003).

A. Nakamoto, K. Nakayama, T. Shintani, Y. Maruya, K. Komai, T. Ishida and Y. Makiguchi, Adaptive management in Kushiro Wetland in the context of salt wedge intrusion due to sea level rise, Hydrological Research Letters 7, 1-5 (2013).

K. Nakayama and J. Imberger, Residual circulation due to internal waves shoaling on a slope, Limnol. Oceanogr. 55, 1009-1023 (2010).

K. Nakayama, T. Shintani, K. Kokubo, T. Kakinuma, Y. Maruya, K. Komai and T. Okada, Residual current over a uniform slope due to breaking of internal waves in a two-layer system, J. Geophys. Res. 117, C10002 doi:10.1029/2012JC008155 (2012).

K. Nakayama, T. Shintani, K. Shimizu, T. Okada, H. Hinata and K. Komai, Horizontal and residual circulations driven by wind stress curl in Tokyo Bay, J. Geophys. Res. 119, 1977-1992 (2014).

K. Nakayama, H.D. Nguyen, T. Shintani and K. Komai, Reversal of secondary circulations in a sharp channel bend, Coastal Engineering Journal 58, 1650002 (2016).

K. Nakayama, T. Kakinuma and H. Tsuji, Oblique reflection of large internal solitary waves in a two-layer fluid, Euro. J. Mech. B/Fluids, Vol. 74, pp. 81-91 (2019a).

K. Nakayama, T. Sato, K. Shimizu and L. Boegman, Classification of internal solitary wave breaking over a slope, Phy. Rev. Fluids, 4, 014801 (2019b).

D. C. Pierson and G. A. Weyhenmeyer, High resolution measurements of sediment resuspension above an accumulation bottom in a stratified lake, Hydrobiologia 284, 43-57, doi:10.1007/BF00005730 (1994).

J. Pineda, Internal tidal bores in the nearshore: Warm-water fronts, seaward gravity currents and the onshore transport of neustonic larvae, J. Mar. Res. 52, 427-458, doi:10.1357/0022240943077046 (1994).

D. P. Renouard, G. C. D'Hières and X. Zhang, An experimental study of strongly nonlinear waves in a rotating system, J. Fluid Mech. 177, 381-394 (1987).

A. Scotti and J. Pineda, Observation of very large and steep internal waves of elevation near the Massachusetts coast, Geophys. Res. Lett. 31, L22307, doi:10.1029/2004GL021052 (2004).

K. Shimizu and K. Nakayama, Effects of topography and earth’s rotation on the oblique interaction of internal solitary-like waves in the Andaman Sea, J. Geophys. Res., 1227449-7465 (2017).

B. Steinman, W. Eckert, S. Kaganowsky and T. Zohary, Seiche-induced resuspension in Lake

Kinneret: A fluorescent tracer experiment, Water Air Soil Poll. 99, 123-131 (1997).

R. Stocker and J. Imberger, Energy partitioning and horizontal dispersion in a stratified rotating lake, J. Phys. Oceanogr. 33, 512-529 (2003).

B. R. Sutherland, K. J. Barrett and G. N. Ivey, Shoaling internal solitary waves, J. Geophys. Res. 118, 4111–4124, doi:10.1002/jgrc.20291 (2013).

S. A. Thorpe, On the shape and breaking of finite amplitude internal gravity waves in a shear flow, J. Fluid Mech. 85, 7–31 (1978).

D. S. Ullman and D. L. Codiga, Seasonal variation of a coastal jet in the Long Island Sound outflow region based on HF radar and Doppler current observations, J. Geophys. Res. 109, C07S06, doi:10.1029/2002JC001660 (2004).

H. N. Ulloa, K. B. Winters, A. de la Fuente and Y. Niño, Degeneration of internal Kelvin waves in a continuous two-layer stratification, J. Fluid Mech. 777, 68–96 (2015).

L. Umlauf and H. Burchard, A generic length-scale equation for geophysical turbulence models, J. Mar. Res. 61, 235-265 (2003).

R. Valipour, D. Bouffard, L. Boegman and Y.R. Rao, Near-inertial waves in Lake Erie, Limnol. Oceanogr., 60, 1522–1535 (2015).

R. Valipour, Y.R. Rao, L.F. León and D. Depew, Nearshore-offshore exchanges in multi-basin coastal waters: Observations and three-dimensional modeling in Lake Erie, J. Great Lakes Res. 45, 50-60 (2019).

G. W. Wake, G. N. Ivey, J. Imberger, N. R. McDonald and R. Stocker, Baroclinic geostrophic adjustment in a rotating circular basin, J. Fluid Mech. 515, 63–86 (2004).

G. W. Wake, G. N. Ivey and J. Imberger, The temporal evolution of baroclinic basin-scale waves in a rotating circular basin, J. Fluid Mech. 523, 367–392 (2005a).

G. W. Wake, G. N. Ivey, J. Imberger and N. R. McDonald, The temporal evolution of a geostrophic flow in a rotating stratified basin, Dynam. Atmos. Ocean. 39, 189–210 (2005b).

R. K. Walter, C. B. Woodson, R. S. Arthur, O. B. Fringer and S. G. Monismith, Nearshore internal bores and turbulent mixing in southern Monterey Bay, J. Geophys. Res. 117, C07017 (2012).

J. Wang, L. A. Mysak and R. G. Ingram, A three-dimensional numerical simulation of Hudson Bay summer ocean circulation: topographic gyres, separations and coastal jets, J. Phys. Oceanogr. 24, 2496-2514 (1994).

A. Wüest and A. Lorke, Small-scale hydrodynamics in lakes, Annu. Rev. Fluid Mech. 35, 373-412 (2003).

Figure captions:

Figure 1 Schematic diagram of the (a) computational domain and (b) laboratory experiment tank.

Figure 2 PIV particle and density distributions without the Coriolis effect under case A at y = 0.005 m. PIV particle distributions in the laboratory experiments at (a) t = 54 s, (b) t = 58 s and (c) t = 60 s. Density distributions in the numerical computations at (d) t = 54 s, (e) t = 58 s and (f) t = 60 s. Green squares indicate the PIV analysis region corresponding to Figures 2a, 2b and 2c.

Figure 3 PIV particle and density distributions with the Coriolis coefficient of 4π/30 (s^{-1}) under case B2A at y = 0.005 m. PIV particle distributions in the laboratory experiments at (a) t = 54 s, (b) t = 58 s and (c) t = 60 s. Density distributions in the numerical computations at (d) t = 54 s, (e) t = 58 s and (f) t = 60 s. Green squares indicate the PIV analysis region corresponding to Figures 3a, 3b and 3c.

Figure 4 Velocity vectors without the Coriolis effect under case A at y = 0.005 m. PIV analysis in the laboratory experiments at (a) t = 54 s, (b) t = 58 s and (c) t = 60 s. Numerical computations at (d) t = 54 s, (e) t = 58 s and (f) t = 60 s. Green squares indicate the PIV analysis region corresponding to Figures 4a, 4b and 4c.

Figure 5 Velocity vectors with the Coriolis coefficient of 4π/30 s^{-1} under case B2 at y = 0.005 m. PIV analysis in the laboratory experiments at (a) t = 54 s, (b) t = 58 s and (c) t = 60 s. Numerical computations at (d) t = 54 s, (e) t = 58 s and (f) t = 60 s. Green squares indicate the PIV analysis region corresponding to Figures 5a, 5b and 5c. (g) Horizontal velocity at x = 3.45 m and z = 0.15 m.

Figure 6 Spanwise pycnocline displacement when breaking points appear at the lateral wall (thick solid lines), at y = 0.1 m (thin solid lines) and at y = 0.2 m (broken lines). Green circles indicate breaking points. (a) case A: no Coriolis effect, (b) case B1: Coriolis coefficient of 4π/20 s^{-1}, (c) case B2: Coriolis coefficient of 4π/30 s^{-1} and (d) case B3: Coriolis coefficient of 4π/40.

Figure 7 Phase averaged density distribution for one IKW period at the lateral wall (a) case A: no Coriolis effect, (b) case B1: Coriolis coefficient of 4π/20 s^{-1}, (c) case B3: Coriolis coefficient of 4π/40 s^{-1} and (d) case B5: Coriolis coefficient of 4π/160 s^{-1}.

Figure 8 Residual current adjacent to the lateral wall. Solid lines indicate phase-averaged pycnocline elevation for one IKW. (a) case A: no Coriolis effect, (b) case B1: Coriolis coefficient of 4π/20 s^{-1}, (c) case B3: Coriolis coefficient of 4π/40 s^{-1} and (d) case B5: Coriolis coefficient of 4π/160 s^{-1}.

Figure 9 Residual current at z = 0.15 m of (a) case A: without the Coriolis effect, (b) case B3: with a Coriolis coefficient of 4π/40 s^{-1}. Residual current adjacent to the slope of (c) case A: no Coriolis effect, and (d) case B3: Coriolis coefficient of 4π/40 s^{-1}.

Figure 10 Comparisons of u_B between computations and theoretical solutions at x = 3.5 m.

Figure 11 Normalized amplitude, a_0 / a_C, and η_{B0} / a_C.

Table caption

Table 1 Computational conditions. The upper- and lower-layer depths were 0.15 m and 0.15 m, respectively, ε was 0.02, the period of an IKW was 10.0 s, and the width of the tank was 0.4 m.

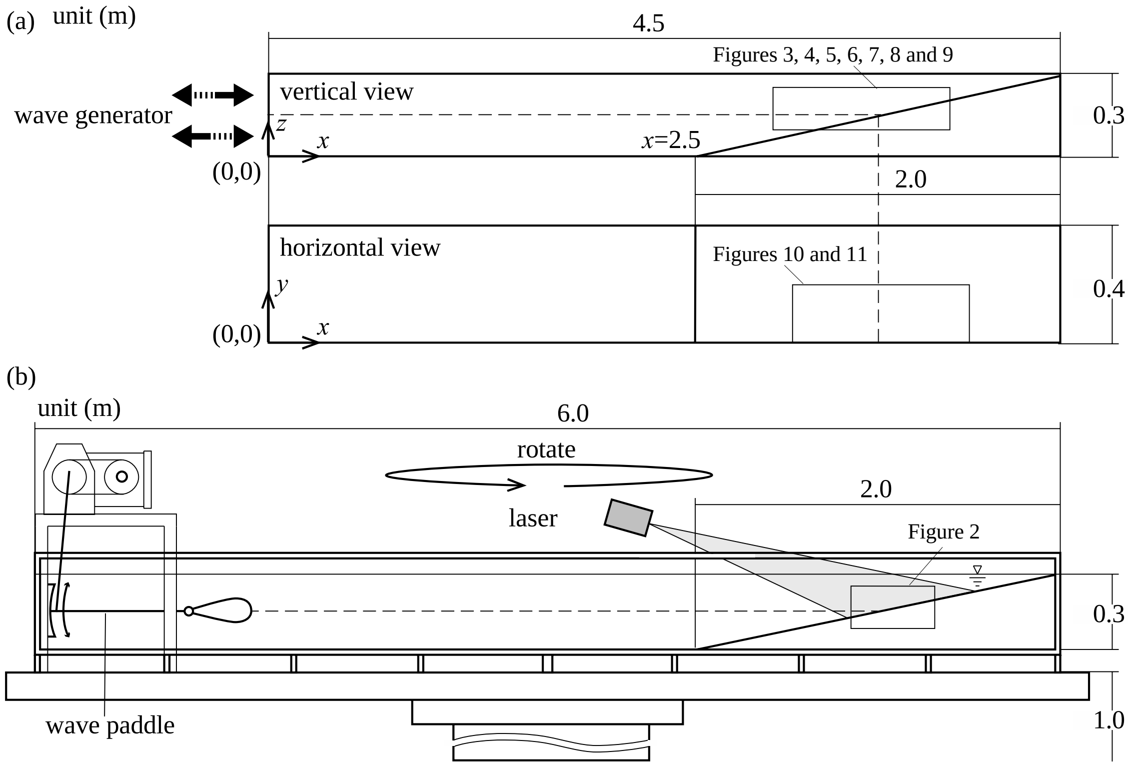

Figure 1 Schematic diagram of the (a) computational domain and (b) laboratory experiment tank.

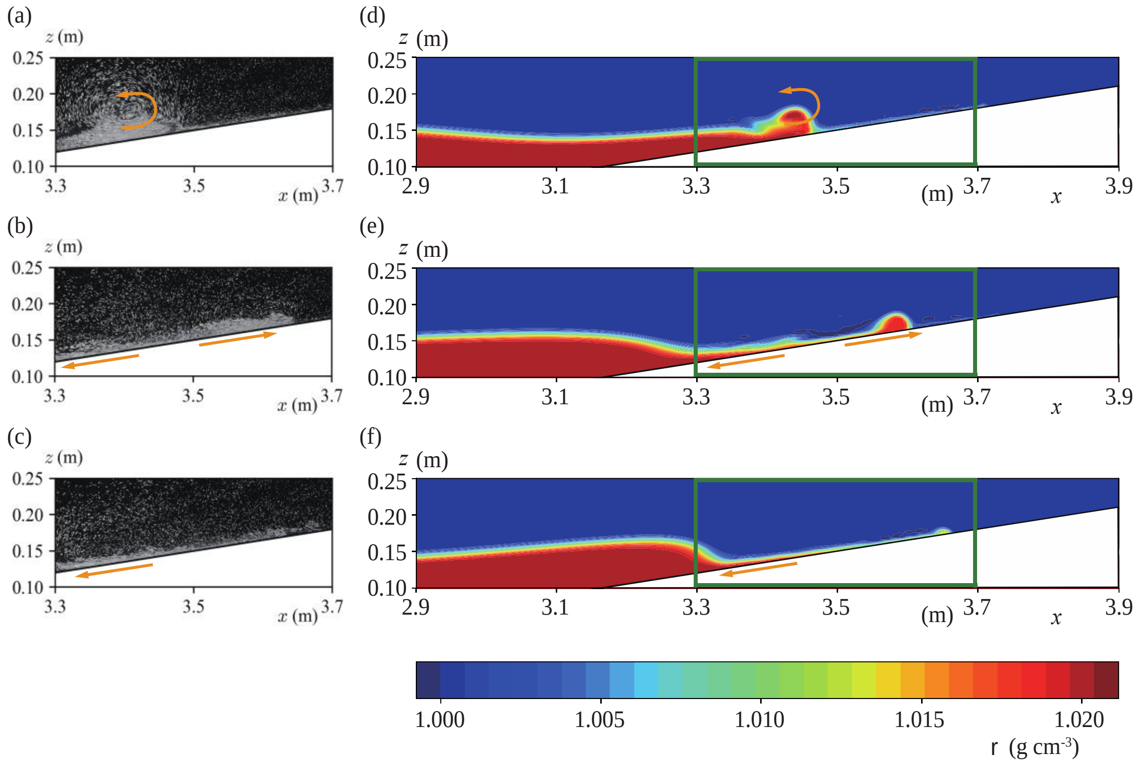

Figure 2 PIV particle and density distributions without the Coriolis effect under case A at y = 0.005 m. PIV particle distributions in the laboratory experiments at (a) t = 54 s, (b) t = 58 s and (c) t = 60 s. Density distributions in the numerical computations at (d) t = 54 s, (e) t = 58 s and (f) t = 60 s. Green squares indicate the PIV analysis region corresponding to Figures 2a, 2b and 2c.

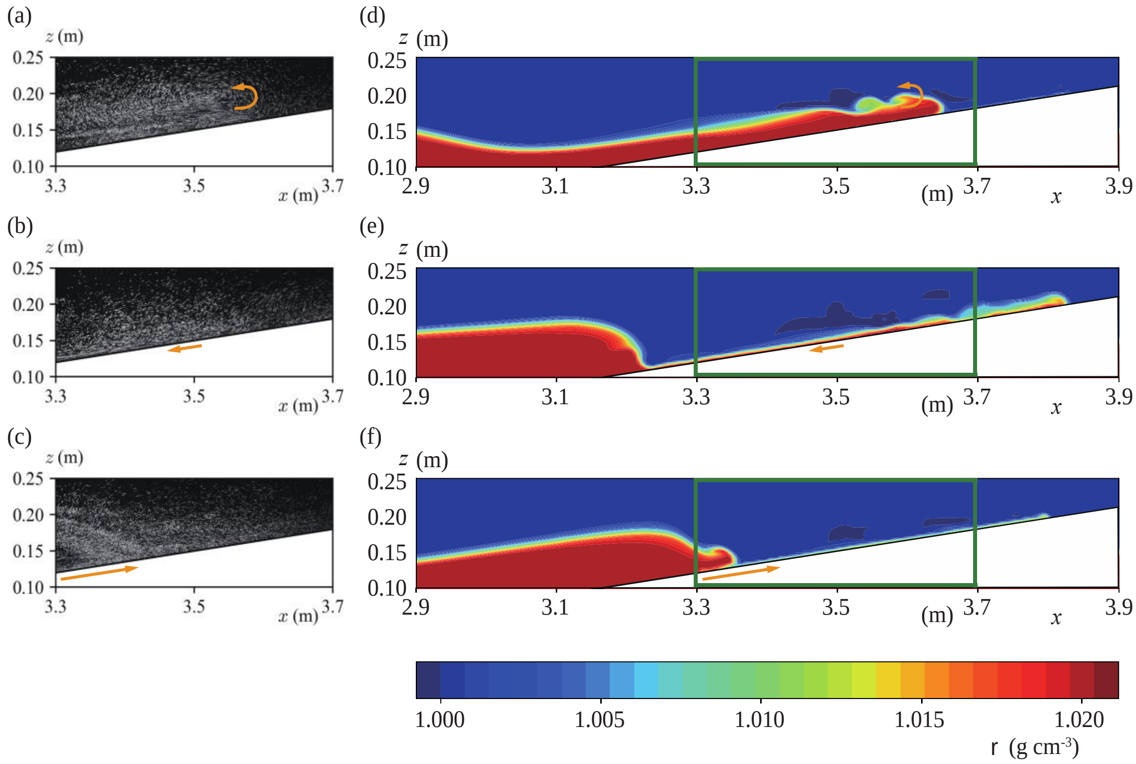

Figure 3 PIV particle and density distributions with the Coriolis coefficient of $4\pi/30$ (s^{-1}) under case B2A at y = 0.005 m. PIV particle distributions in the laboratory experiments at (a) t = 54 s, (b) t = 58 s and (c) t = 60 s. Density distributions in the numerical computations at (d) t = 54 s, (e) t = 58 s and (f) t = 60 s. Green squares indicate the PIV analysis region corresponding to Figures 3a, 3b and 3c.

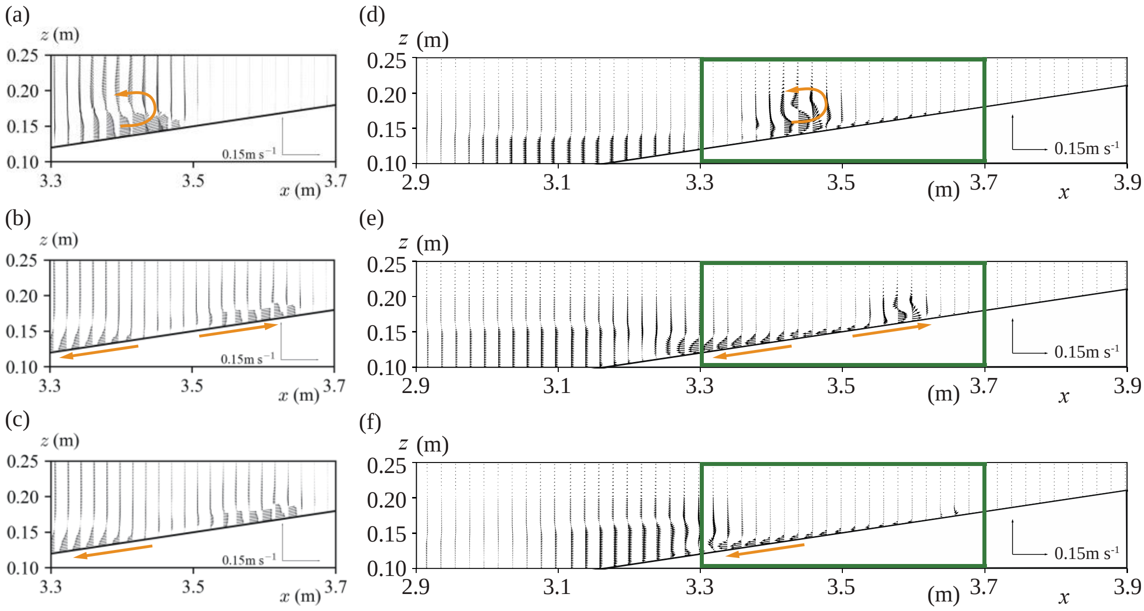

Figure 4 Velocity vectors without the Coriolis effect under case A at y = 0.005 m. PIV analysis in the laboratory experiments at (a) t = 54 s, (b) t = 58 s and (c) t = 60 s. Numerical computations at (d) t = 54 s, (e) t = 58 s and (f) t = 60 s. Green squares indicate the PIV analysis region corresponding to Figures 4a, 4b and 4c.

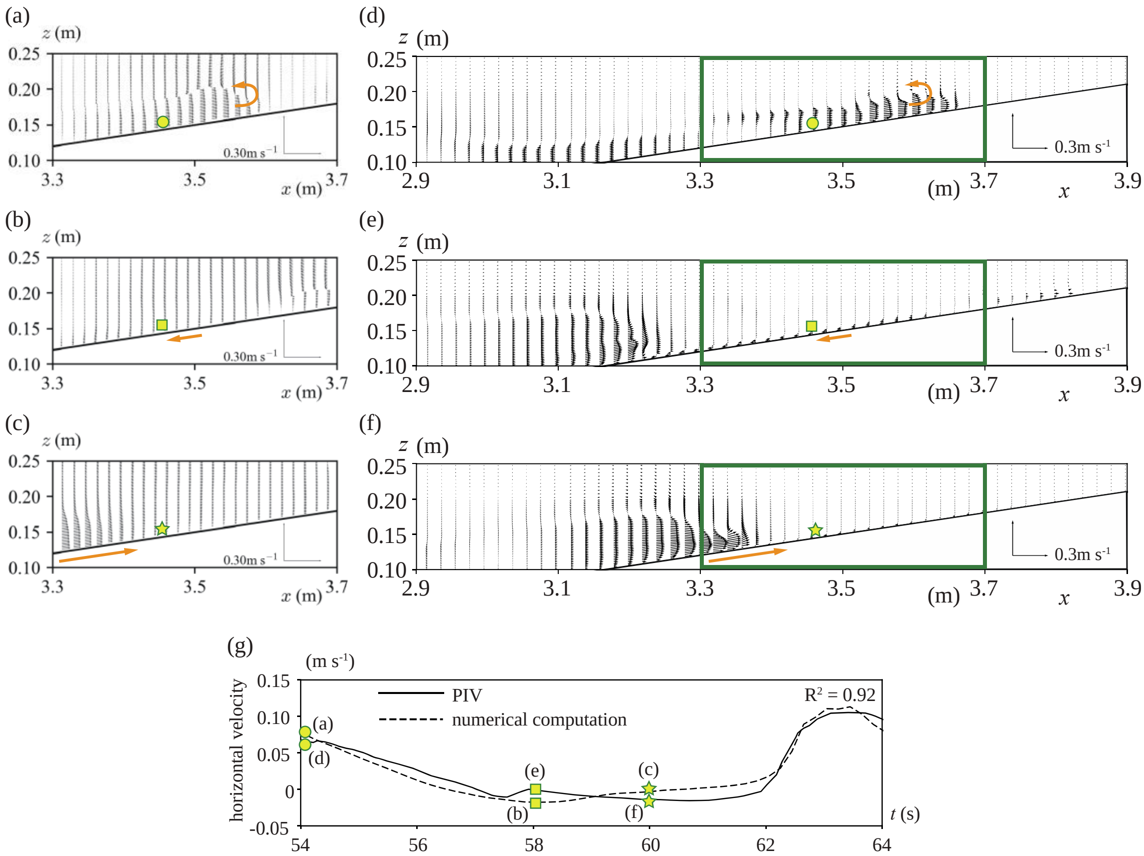

Figure 5 Velocity vectors with the Coriolis coefficient of 4π/30 s^{-1} under case B2 at y = 0.005 m. PIV analysis in the laboratory experiments at (a) t = 54 s, (b) t = 58 s and (c) t = 60 s. Numerical computations at (d) t = 54 s, (e) t = 58 s and (f) t = 60 s. Green squares indicate the PIV analysis region corresponding to Figures 5a, 5b and 5c. (g) Horizontal velocity at x = 3.45 m and z = 0.15 m.

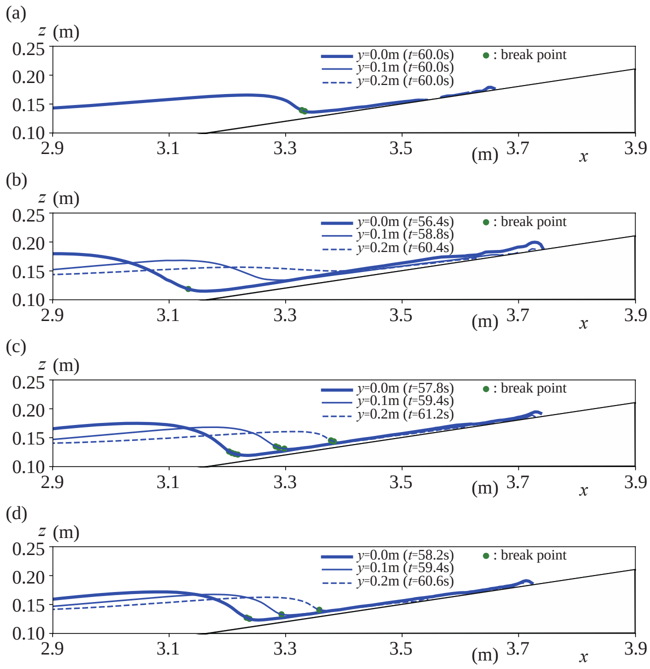

Figure 6 Spanwise pycnocline displacement when breaking points appear at the lateral wall (thick solid lines), at y = 0.1 m (thin solid lines) and at y = 0.2 m (broken lines). Green circles indicate breaking points. (a) case A: no Coriolis effect, (b) case B1: Coriolis coefficient of $4\pi/20$ s^{-1}, (c) case B2: Coriolis coefficient of $4\pi/30$ s^{-1} and (d) case B3: Coriolis coefficient of $4\pi/40$.

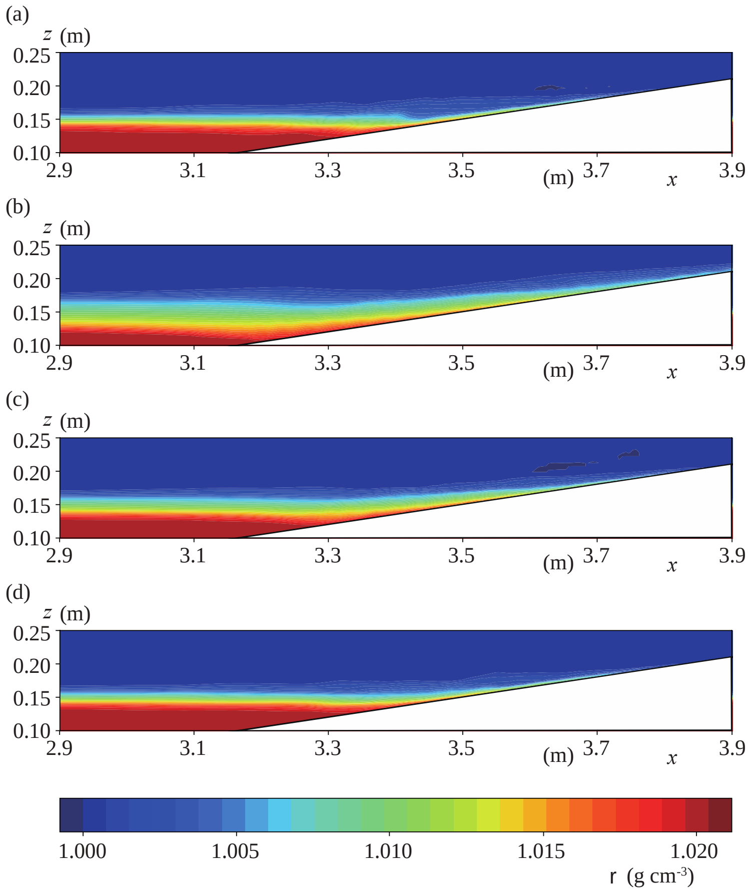

Figure 7 Phase averaged density distribution for one IKW period at the lateral wall (a) case A: no Coriolis effect, (b) case B1: Coriolis coefficient of $4\pi/20\ s^{-1}$, (c) case B3: Coriolis coefficient of $4\pi/40\ s^{-1}$ and (d) case B5: Coriolis coefficient of $4\pi/160\ s^{-1}$.

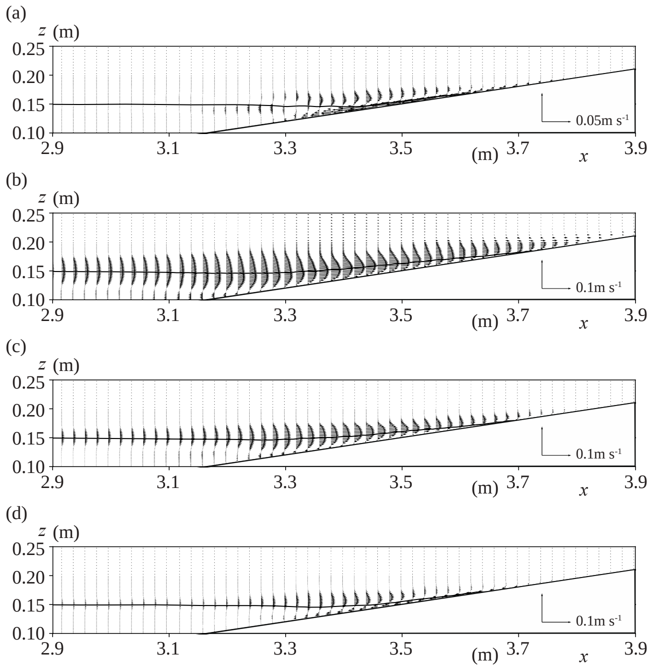

Figure 8 Residual current adjacent to the lateral wall. Solid lines indicate phase-averaged pycnocline elevation for one IKW. (a) case A: no Coriolis effect, (b) case B1: Coriolis coefficient of $4\pi/20\ s^{-1}$, (c) case B3: Coriolis coefficient of $4\pi/40\ s^{-1}$ and (d) case B5: Coriolis coefficient of $4\pi/160\ s^{-1}$.

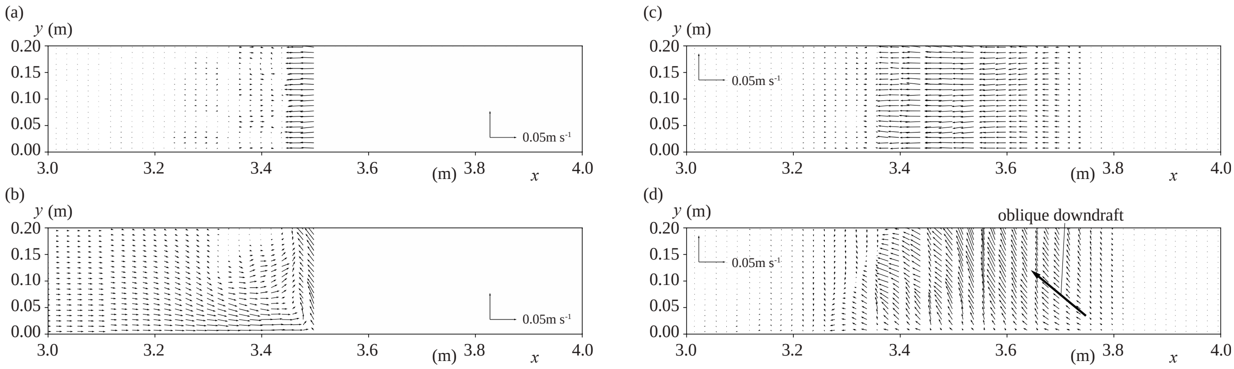

Figure 9 Residual current at z = 0.15 m of (a) case A: without the Coriolis effect, (b) case B3: with a Coriolis coefficient of $4\pi/40\ s^{-1}$. Residual current adjacent to the slope of (c) case A: no Coriolis effect, and (d) case B3: Coriolis coefficient of $4\pi/40\ s^{-1}$.

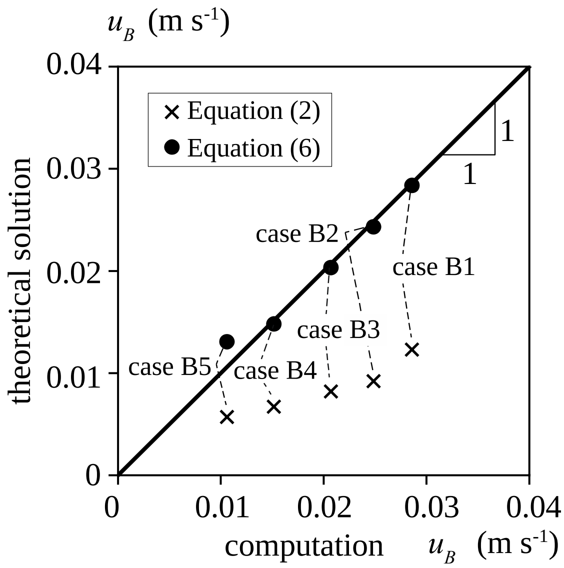

Figure 10 Comparisons of u_B between computations and theoretical solutions at x = 3.5 m.

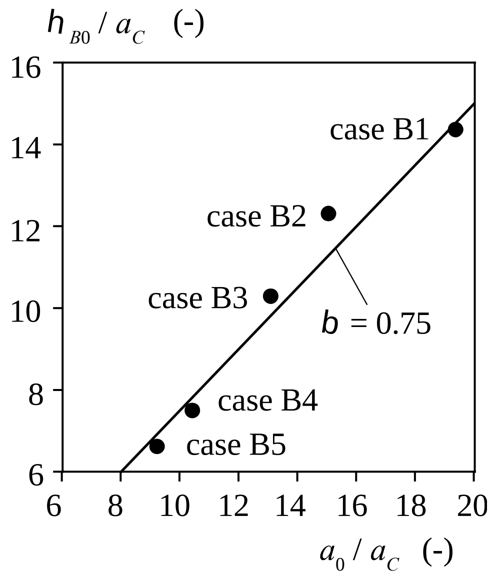

Figure 11 Normalized amplitude, a_0 / a_C , and η_{B0} / a_C.

Table 1 Computational conditions. The upper- and lower-layer depths were 0.15 m and 0.15 m, respectively, ε was 0.02, the period of an IKW was 10.0 s, and the width of the tank was 0.4 m.

	f_C (s^{-1})	λ_I (m)	a_0 (m)	η_{B0} (m)	u_B (m s^{-1})
case A	-	-	0.010	-	-
case B1	4π/20	0.19	0.024	0.018	0.029
case B2	4π/30	0.29	0.018	0.015	0.025
case B3	4π/40	0.39	0.016	0.013	0.021
case B4	4π/80	0.77	0.013	0.009	0.015
case B5	4π/160	1.54	0.011	0.008	0.011